

A semi-implicit two dimensional solver for a covariant formulation of the shallow water equations

Maurizio Tavelli^a, Olindo Zanotti^b

^a*Department of Engineering for Innovation Medicine, University of Verona, Strada le Grazie 15, Verona, 37134, Italy*

^b*Laboratory of Applied Mathematics, DICAM, University of Trento, via Mesiano 77, 38123 Trento, Italy*

Abstract

In this paper we combine a flexible covariant formulation of the shallow water equations with the semi-implicit numerical scheme developed over the years by Casulli and collaborators. After adopting an orthogonal, but non-orthonormal, coordinate basis on two dimensional manifolds, and by writing the divergence of symmetric tensors in a way that avoids the introduction of Christoffel symbols, the shallow water equations preserve a very close resemblance to the usual one expressed in Cartesian coordinates. In this way, a stable semi-implicit scheme can be derived by using an implicit discretization for the gradient of surface elevation in the momentum equations and for the velocity in the continuity equation, with stability properties that are independent of the celerity. We have tested the new method over a variety of challenging benchmarks, including, among the others, the smooth wave propagation over a water globe and the deformation of an artery branch. Two appealing additional features make the method particularly powerful with respect to oceanographic applications: firstly, thanks to the wetting and drying ability of our semi-implicit approach, no pathological behaviors occur at the poles; secondly, the scheme is naturally well-balanced, and it is able to preserve perfect stationarity, up to machined precision, of the entire ocean configuration of the earth.

Keywords: Shallow water equations, covariant formulation, semi-implicit schemes

1. Introduction

In spite of representing a crude simplification with respect to the Navier Stokes equations for fluid dynamics, the shallow water equations still attract a lot of interest, for their effectiveness in modeling various kinds of free surface flows under quite different physical and morphological conditions. The scientific literature on the subject is actually so large that it is virtually impossible to cover in a few sentences the advancements that have been performed, both with respect to the variety of applications and with respect to the numerical schemes that have been developed. We just mention that a very prominent application is represented by tsunami wave propagation, for which high order numerical schemes were proposed by [Castro et al. \(2012\)](#). We address the interested reader to a few excellent reviews of this topic, such as those presented by [Casulli and Zanotti \(2022\)](#); [Delis and Nikolos \(2021\)](#); [García-Navarro et al. \(2019\)](#); [Toro \(2024\)](#); [Ndengna Ngatcha \(2024\)](#).

Among the large family of numerical schemes that have been developed over the years for the solution of the shallow water equations, semi-implicit schemes on staggered grids represent a notable case. They were first developed on Cartesian meshes by [Casulli \(1990\)](#) and then extended to unstructured ones in [Casulli and Walters \(2000\)](#). The shallow water system is characterized by the coexistence of several different scales. Pressure waves travel at a speed given by the celerity \sqrt{gH} , which can become considerably large

Email addresses: maurizio.tavelli@univr.it (Maurizio Tavelli), olindo.zanotti@unitn.it (Olindo Zanotti)

depending on the value of the total water height H . The advective part, on the contrary, is governed by the fluid velocity, which is typically much smaller. In these conditions, a standard explicit scheme would be limited by a severe CFL condition (Courant et al., 1928) driven by the fastest wave speeds, i.e. the celerity. On the contrary, semi-implicit methods on staggered meshes perform an implicit discretization of a few crucial quantities that are carefully selected to obtain a simple non linear system to be solved at each time iteration. More specifically, Casulli (1990) showed that it is possible to obtain a simple non-linear system whose non-linearities appear only on the diagonal, while the linear part is provably symmetric and positive semi-definite. Over the years, this methodology has been extended both to more advanced high order methods (Dumbser and Casulli, 2013; Tavelli and Dumbser, 2014) and to challenging PDE systems (Brugnano and Casulli, 2009; Casulli et al., 2012b; Tavelli et al., 2013; Lucca et al., 2023, 2025; Dumbser et al., 2026).

When the shallow water equations need to be solved on curved geometries, like in oceanographic applications where the earth curvature cannot be neglected (Kolar et al., 1994; Li and Xiao, 2010; Zeitlin, 2007; Ringler et al., 2010), or even in blood flows within arteries, curvilinear coordinates must be adopted. In this respect, the mathematical tools borrowed from differential geometry turn out to be very convenient, and covariant formulations of the shallow water equations become necessary. Several promising attempts have already been proposed, such as, among the others, those of Kolar et al. (1994), Wintermeyer et al. (2017), Arpaia et al. (2022), Carlino and Gaburro (2023), Montoya et al. (2026), where a variety of discretization techniques have been explored.

Our approach for the solution of the shallow water equations on curved manifolds is based on two key features. Firstly, we adopt a particularly simple covariant version of the shallow water equations in two space dimensions, which fully exploits the tensor expression of the divergence operator. The net result of this simple gimmick is that no Christoffel symbols appear in the equations, which therefore maintain the closest possible resemblance of their Cartesian counterpart. As a side effect, the evolved quantities acquire the geometric factor $\sqrt{\gamma}$ (γ being the determinant of the curved manifold in the specific coordinates adopted), while an extra algebraic source term appears on the right hand side. When the coordinates are Cartesian, $\gamma = 1$, covariant and contra-variant components of any tensor coincide, and the covariant form of the equations naturally reduces to the usual expressions. Secondly, we extend the semi-implicit schemes introduced by Casulli (1990); Casulli and Walters (2000) to this new formulation, preserving all of their numerical advantageous properties. In particular, the semi-implicit approach, removes the pathological effects due to coordinate singularities, such as those affecting the poles on a spherical surface. Moreover, the numerical scheme is also naturally well balanced, in the sense of Castro et al. (2008, 2017b,a); Castro and Parés (2020), as already proved by Boscheri et al. (2023b).

We have validated the new approach over a number of crucial tests for the classical shallow water equations, including: the propagation of a smooth wave over waterland across the poles, the well balanced property of the entire earth oceans, two standard Riemann problem, the simulation of a steady state geostrophic flow and the simulation of blood flow in an artery with deformation.

The plan of the paper is the following: in Sect. 2 we present the governing equations of shallow water written in a particular simple covariant form that avoids Christoffel symbols. Sect. 3 is instead devoted to the presentation of the semi-implicit numerical scheme. Sect. 4 contains the numerical results of our investigation, and Sect. 5 concludes our work. Regarding the notation, we make an important distinction among tensor indices and discretization indices:

- Indices i and j are *only* used as spatial discretization indices. appearing as subscripts.
- Index n is *only* used as temporal discretization index. appearing as superscript.
- Greek indices α, β, μ and ν are *only* used as tensor indices, ranging from 1 to 2, appearing either covariant or contra-variant.

Moreover, we adopt the standard Einstein summation convention over repeated (tensor) indices. Finally we

adopt the standard IS system of units all along the paper. In this context, especially on very large scales, it is critical to adopt a proper normalization of the involved equations, as detailed in Section 3.5.

2. The covariant formulation of the Shallow Water equations

2.1. Choice of the curvilinear coordinates

We plan to solve the shallow water equations written in covariant form, assuming that the acceleration vector \vec{g} is locally perpendicular to a two-dimensional manifold. The manifold itself is covered by a single coordinate chart, and the coordinates are denoted as x^α , with $\alpha = 1, 2$. Using more than one chart is in principle possible but we will not consider this case here. The covariant spatial metric is given by $\gamma_{\alpha\beta}$, which can be represented as a 2×2 symmetric matrix, which allows to compute physical distances on the manifold from

$$dl^2 = \gamma_{\alpha\beta} dx^\alpha dx^\beta = \gamma_{11}(dx^1)^2 + \gamma_{22}(dx^2)^2, \quad (1)$$

where we have assumed, as it will be done hereafter, that the metric is diagonal. Since a natural application of the shallow water equations occur on the surface of the earth, two-dimensional spherical coordinates will be often adopted, hence with $x^1 = \theta$, $x^2 = \phi$. In that case we have¹

$$X(\theta, \phi) = R \sin \theta \cos \phi \quad (2)$$

$$Y(\theta, \phi) = R \sin \theta \sin \phi \quad (3)$$

$$Z(\theta, \phi) = R \cos \theta, \quad (4)$$

where R is the radius of the sphere, and the spatial metric becomes simply

$$\gamma_{\alpha\beta}(\theta, \phi, R) = \begin{pmatrix} R^2 & 0 \\ 0 & R^2 \sin^2 \theta \end{pmatrix}, \quad \gamma = \det(\gamma_{\alpha\beta}), \quad (5)$$

with $\sqrt{\gamma} = R^2 \sin \theta$. An alternative example of the metric in cylindrical coordinates, suitable for applications to arterial flows, will be shown in Sect. 3.6.

2.2. Formulation of the equations

The shallow water equations on a curved manifold can be obtained starting from the usual continuity and momentum equations

$$\frac{\partial \rho}{\partial t} + \nabla_\alpha (\rho u^\alpha) = 0 \quad (6)$$

$$\frac{\partial u^\alpha}{\partial t} + u^\beta \nabla_\beta u^\alpha + \nabla_\beta T^{\alpha\beta} = 0, \quad (\alpha, \beta = 1, 2) \quad (7)$$

where $T^{\alpha\beta}$ are the components of the standard stress tensor for a perfect fluid, given by [see Eq. (26.8) by Mihalas and Weibel-Mihalas (1984)], i.e.

$$T^{\alpha\beta} = p \gamma^{\alpha\beta}. \quad (8)$$

Now, we first introduce the total water depth $H = \eta - b$, where η is the water surface elevation and b the prescribed bathymetry. Then, recalling the usual assumptions of the shallow water approximation, namely:

- Incompressibility: $\nabla_\beta u^\beta = 0$;

¹Note that θ is measured from the vertical axis, hence it is a polar angle.

- Integration along the local normal to the manifold (henceforth referred to as *vertical averaging*) of any quantity along the z direction, such that, for instance, $v^\alpha = \frac{1}{H} \int_b^\eta u^\alpha dz$;
- Hydrostatic vertical equilibrium, such that $p = p_e + g(\eta - z)$, where p has been normalized by the constant ρ , and where p_e is the external pressure,

it is possible to show that Eq. (6)-(7) transform into (see [Appendix A](#) for the derivation)

$$\frac{\partial(\sqrt{\gamma}H)}{\partial t} + \partial_\beta(\sqrt{\gamma}m^\beta) = 0, \quad (9)$$

$$\frac{\partial(\sqrt{\gamma}m_\alpha)}{\partial t} + \partial_\beta\left(\sqrt{\gamma}\frac{m_\alpha m^\beta}{H}\right) + g\sqrt{\gamma}H\partial_\alpha\eta = \frac{1}{2}\sqrt{\gamma}\left[\frac{m^\mu m^\nu}{H}\partial_\alpha\gamma_{\mu\nu}\right], \quad (10)$$

where we have defined the mass flux as $m^\alpha = Hv^\alpha$. Note that one has to distinguish among the coordinate velocity $u^\alpha = dx^\alpha/dt$ and the physical velocity $|\vec{u}| = \sqrt{\gamma_{\alpha\beta}u^\alpha u^\beta}$. For convenience we may write $\tilde{H} = \sqrt{\gamma}H$ and $\tilde{m}_\alpha = \sqrt{\gamma}m_\alpha$, and we emphasize that, even if η may assume values smaller than b , the total water depth is in general a non linear function of η , namely: $H(\eta) = \max(0, \eta - b)$. Hence, a non linearity is introduced in order to allow for wetting (when $\eta > b$) and also for drying (when $\eta < b$). In this last case we simply obtain $H(\eta) = 0$ and no momentum equation need to be solved, i.e. $m_\alpha = 0$. See also [Casulli \(2009\)](#). The previous system then reads

$$\partial_t\tilde{H} + \partial_\beta\tilde{m}^\beta = 0, \quad (11)$$

$$\partial_t\tilde{m}_\alpha + \partial_\beta(\tilde{m}_\alpha v^\beta) + \underbrace{g\tilde{H}\partial_\alpha\eta}_{\text{pressure gradients}} = \underbrace{\frac{1}{2}\tilde{m}^\mu v^\nu \partial_\alpha\gamma_{\mu\nu}}_{\text{curvature correction}}. \quad (12)$$

If we compare Eq. (11)-(12) above with Eq. (11) by [Casulli and Zanolli \(2022\)](#) we can see that the two expressions are formally very close to each other. As a matter of fact, the curvature effects are entirely accounted for by the first term on the right hand side of (12), by the factor $\sqrt{\gamma}$, as well as by the crucial distinction among covariant and contravariant vector components. For example, while in the continuity equation (11) the momentum field \tilde{m}^β enters as a contravariant vector, in the momentum equation (11) it appears as a covariant one. We change from one form to the other through the metric as

$$\tilde{m}^\mu = \gamma^{\mu\nu}\tilde{m}_\nu. \quad (13)$$

Since the metric is diagonal, this amounts to

$$\tilde{m}^1 = \gamma^{11}\tilde{m}_1 = \frac{\tilde{m}_1}{\gamma_{11}}, \quad \tilde{m}^2 = \gamma^{22}\tilde{m}_2 = \frac{\tilde{m}_2}{\gamma_{22}}. \quad (14)$$

2.3. Inclusion of the Coriolis force

For rotating systems like the earth, it is necessary to include also the non-inertial effects due to the Coriolis force. In vector form, the Coriolis acceleration in the corotating frame is $\vec{a}_C = -2\vec{\Omega} \times \vec{v}$. In components, this can be written as:

$$(a_C)^\alpha = -2\epsilon^{\alpha\beta\gamma}\Omega_\beta v_\gamma, \quad (15)$$

where $\epsilon^{\alpha\beta\gamma}$ is the Levi-Civita tensor, which has components $\epsilon^{\alpha\beta\gamma} = 1/\sqrt{\gamma} \cdot [\alpha\beta\gamma]$, and where $[\alpha\beta\gamma]$ are the totally antisymmetric symbols. Having in mind applications on the earth surface using coordinates (θ, ϕ) , the two relevant components of the Coriolis acceleration are

$$(a_C)^\theta = \frac{2}{\sqrt{\gamma}}\Omega_r v_\phi = \frac{2}{\sqrt{\gamma}}\cos\theta\Omega v_\phi \quad (16)$$

$$(a_C)^\phi = -\frac{2}{\sqrt{\gamma}}\Omega_r v_\theta = -\frac{2}{\sqrt{\gamma}}\cos\theta\Omega v_\theta, \quad (17)$$

where the angular velocity vector $\vec{\Omega}$ is oriented along the z axis. As shown by [Casulli and Walters \(2000\)](#), Coriolis terms ought to be treated implicitly. This means that, if we focus just on Coriolis corrections to the momentum equation (12), and after introducing the *Coriolis parameter* as $f = 2\cos\theta\Omega$, the numerical discretization of the Coriolis correction will be

$$v^{1,n+1} = v^{1,fl} + \Delta t \frac{f}{\sqrt{\gamma}} v_2^{n+1} = v^{1,fl} + \Delta t \frac{f}{\sqrt{\gamma_{11}} \sqrt{\gamma_{22}}} \gamma_{22} v^{2,n+1} \quad (18)$$

$$v^{2,n+1} = v^{2,fl} - \Delta t \frac{f}{\sqrt{\gamma}} v_1^{n+1} = v^{2,fl} - \Delta t \frac{f}{\sqrt{\gamma_{11}} \sqrt{\gamma_{22}}} \gamma_{11} v^{1,n+1} \quad (19)$$

which amounts to

$$v^{1,n+1} = v^{1,fl} + \Delta t f \sqrt{\frac{\gamma_{22}}{\gamma_{11}}} v^{2,n+1} \quad (20)$$

$$v^{2,n+1} = v^{2,fl} - \Delta t f \sqrt{\frac{\gamma_{11}}{\gamma_{22}}} v^{1,n+1}, \quad (21)$$

where $v^{1,fl}$ and $v^{2,fl}$ are the components of the advection contribution, see Section 3.4. Note that (20)-(21) collapse to the same expression found by [Casulli and Walters \(2000\)](#) if an Euclidean metric is considered. The previous system can easily be inverted in the unknowns $v^{\alpha,n+1}$ and reads

$$v^{1,n+1} = \frac{1}{1 + \Delta t^2 f^2} \left(v^{1,fl} + f \Delta t \sqrt{\frac{\gamma_{22}}{\gamma_{11}}} v^{2,fl} \right) \quad (22)$$

$$v^{2,n+1} = \frac{1}{1 + \Delta t^2 f^2} \left(v^{2,fl} - f \Delta t \sqrt{\frac{\gamma_{11}}{\gamma_{22}}} v^{1,fl} \right). \quad (23)$$

3. Semi implicit numerical scheme

3.1. Staggered meshes for the reference space

We discretize a reference two dimensional domain Ω_R using a simple uniform mesh. As stated above, we then assume that the metric tensor $\gamma_{\alpha\beta}$ is diagonal, meaning that the coordinate basis is orthogonal. This is an extension of the concept of unstructured orthogonal meshes introduced by [Casulli and Walters \(2000\)](#). See also [Tavelli and Dumbser \(2014\)](#). For convenience of notation, and in order to help the comparison with already existing algorithms, in this Section we assume $x^1 = x$ and $x^2 = y$. We cover the coordinate space Ω_R with $N_x \times N_y$ segments in the x and y direction, respectively. Each center is identified with the coordinates x_i and y_j for $i = 1 \dots N_x$, $j = 1 \dots N_y$. We then use two edge-based *staggered grids* that are identified with the half indices, namely the center of any vertical edge is written as $(x_{i+\frac{1}{2}}, y_j)$ and $(x_i, y_{j+\frac{1}{2}})$ for the horizontal faces. We then call $\Delta x = x_{i+\frac{1}{2}} - x_{i-\frac{1}{2}}$ and $\Delta y = y_{j+\frac{1}{2}} - y_{j-\frac{1}{2}}$, which are both constant.

3.2. Numerical approximation

As originally proposed by [Casulli \(1990\)](#), the vertically averaged velocity is discretized over the edges while the free surface elevation, the bathymetry and the total water depth are formally defined over the centers. This is often referred to as the *primary* discretization. According to the notation specified at the end of Sect. 1, we use i and j as spatial discretization indices, n as a temporal discretization index, and

Greek letters as tensorial indices. After defining the solution time $t^n = t^{n-1} + \Delta t^n$ as a function of the time interval Δt^n , the corresponding primary numerical quantities are indicated as follows:

$$\eta_{i,j}^n = \eta(x_i, y_j, t^n), \quad b_{i,j} = b(x_i, y_j), \quad \tilde{H}_{i,j}(\eta_{i,j}^n) = \sqrt{\gamma_{i,j}} \max(0, \eta_{i,j}^n - b_{i,j}), \quad (24)$$

$$\tilde{m}_{i+\frac{1}{2},j}^{1,n} = \tilde{m}^1(x_{i+\frac{1}{2}}, y_j, t^n), \quad \tilde{m}_{i,j+\frac{1}{2}}^{2,n} = \tilde{m}^2(x_i, y_{j+\frac{1}{2}}, t^n), \quad \gamma_{i,j}^{\mu\nu} = \gamma^{\mu\nu}(x_i, y_j). \quad (25)$$

All these quantities are assumed to be constant over the elements and edges where they are defined, while the velocity is perpendicular to the edge where it is defined. A schematic view of the adopted discretization

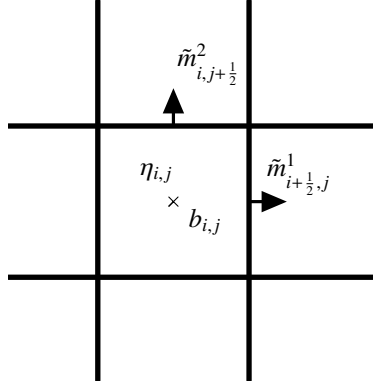


Figure 1: Schematic view of the adopted discretization.

is reported in Fig 1. Analogously, we use the term *dual* discretization to indicate a discretization that is staggered with respect to the primary one. Hence, we compute the corresponding dual components as:

$$\eta_{i+\frac{1}{2},j}^n = \max(\eta_{i,j}^n, \eta_{i+1,j}^n), \quad \eta_{i,j+\frac{1}{2}}^n = \max(\eta_{i,j}^n, \eta_{i,j+1}^n), \quad (26)$$

$$b_{i+\frac{1}{2},j} = \max(b_{i,j}, b_{i+1,j}), \quad b_{i,j+\frac{1}{2}} = \max(b_{i,j}, b_{i,j+1}), \quad (27)$$

$$\gamma_{i+\frac{1}{2},j}^{\mu\nu} = \gamma^{\mu\nu}(x_{i+\frac{1}{2}}, y_j), \quad \gamma_{i,j+\frac{1}{2}}^{\mu\nu} = \gamma^{\mu\nu}(x_i, y_{j+\frac{1}{2}}), \quad (28)$$

$$\tilde{H}(\eta_{i+\frac{1}{2},j}^n) = \sqrt{\gamma_{i+\frac{1}{2},j}} \max(0, \eta_{i+\frac{1}{2},j}^n - b_{i+\frac{1}{2},j}), \quad \tilde{H}(\eta_{i,j+\frac{1}{2}}^n) = \sqrt{\gamma_{i,j+\frac{1}{2}}} \max(0, \eta_{i,j+\frac{1}{2}}^n - b_{i,j+\frac{1}{2}}). \quad (29)$$

A consistent semi-implicit approximation of the continuity equation (11) reads

$$\tilde{H}_{i,j}^{n+1} = \tilde{H}_{i,j}^n - \Delta t \frac{\tilde{m}_{i+\frac{1}{2},j}^{1,n+1} - \tilde{m}_{i-\frac{1}{2},j}^{1,n+1}}{\Delta x} - \Delta t \frac{\tilde{m}_{i,j+\frac{1}{2}}^{2,n+1} - \tilde{m}_{i,j-\frac{1}{2}}^{2,n+1}}{\Delta y}, \quad (30)$$

while a finite difference approximation of the momentum equation reads

$$\tilde{m}_{1,i+\frac{1}{2},j}^{n+1} = F_{1,i+\frac{1}{2},j}^n - g_{i+\frac{1}{2},j}^{n+1} \Delta t \tilde{H}_{i+\frac{1}{2},j}^n \frac{\eta_{i+1,j}^{n+1} - \eta_{i,j}^{n+1}}{\Delta x} \quad (31)$$

$$\tilde{m}_{2,i,j+\frac{1}{2}}^{n+1} = F_{2,i,j+\frac{1}{2}}^n - g_{i,j+\frac{1}{2}}^{n+1} \Delta t \tilde{H}_{i,j+\frac{1}{2}}^n \frac{\eta_{i,j+1}^{n+1} - \eta_{i,j}^{n+1}}{\Delta y}. \quad (32)$$

Here F_1^n and F_2^n are stable approximations of the non-linear convective, Coriolis, and distortion terms. Further forces such as gravity gradients may be added. Since in a spherical coordinate system the distortion close to the poles is very large (due to the factor $\sqrt{\gamma}$), then the velocity field in the reference space can be

huge. Hence an explicit discretization of those terms may be affected from a severe CFL time step restriction for some configurations. In Sect. 3.4, a semi-Lagrangian approach, following an idea originally proposed by [Stelling and Duinmeijer \(2003\)](#), is presented to cope with this potential difficulty. In Eq. (31)-(32) the free surface is discretized implicitly in order to avoid a time restriction driven by the celerity, while the terms \tilde{H} are discretized explicitly to avoid off-diagonal non-linear terms. This approach has been widely adopted after [Casulli \(1990\)](#). After applying the transformation Eq. (14) to the discrete momentum (31)-(32), we replace the obtained quantities in the discrete continuity equation, obtaining a system with the free surface elevation as the only unknown, i.e.

$$\begin{aligned}\tilde{H}_{i,j}^{n+1} &= \tilde{H}_{i,j}^n - \frac{\Delta t}{\Delta x} \left[F_{i+\frac{1}{2},j}^{1,n} - F_{i-\frac{1}{2},j}^{1,n} \right] - \frac{\Delta t}{\Delta y} \left[F_{i,j+\frac{1}{2}}^{2,n} - F_{i,j-\frac{1}{2}}^{2,n} \right] \\ &+ \frac{\Delta t^2}{\Delta x^2} \left[\gamma_{i+\frac{1}{2},j}^{11} g_{i+\frac{1}{2},j}^{n+1} \tilde{H}_{i+\frac{1}{2},j}^n (\eta_{i+1,j}^{n+1} - \eta_{i,j}^{n+1}) - \gamma_{i-\frac{1}{2},j}^{11} g_{i-\frac{1}{2},j}^{n+1} \tilde{H}_{i-\frac{1}{2},j}^n (\eta_{i,j}^{n+1} - \eta_{i-1,j}^{n+1}) \right] \\ &+ \frac{\Delta t^2}{\Delta y^2} \left[\gamma_{i,j+\frac{1}{2}}^{22} g_{i,j+\frac{1}{2}}^{n+1} \tilde{H}_{i,j+\frac{1}{2}}^n (\eta_{i,j+1}^{n+1} - \eta_{i,j}^{n+1}) - \gamma_{i,j-\frac{1}{2}}^{22} g_{i,j-\frac{1}{2}}^{n+1} \tilde{H}_{i,j-\frac{1}{2}}^n (\eta_{i,j}^{n+1} - \eta_{i,j-1}^{n+1}) \right].\end{aligned}\quad (33)$$

The previous system can be written in a compact form as

$$\tilde{H}_{i,j}(\eta_{i,j}^{n+1}, b_{i,j}) + S_{i,j}^n \eta_{i,j}^{n+1} - s_{i+\frac{1}{2},j}^n \eta_{i+1,j}^{n+1} - s_{i-\frac{1}{2},j}^n \eta_{i-1,j}^{n+1} - s_{i,j+\frac{1}{2}}^n \eta_{i,j+1}^{n+1} - s_{i,j-\frac{1}{2}}^n \eta_{i,j-1}^{n+1} = b_{i,j}^n, \quad (34)$$

where

$$s_{i\pm\frac{1}{2},j}^n = \frac{\Delta t^2}{\Delta x^2} \gamma_{i\pm\frac{1}{2},j}^{11} g_{i\pm\frac{1}{2},j}^{n+1} \tilde{H}_{i\pm\frac{1}{2},j}^n, \quad (35)$$

$$s_{i,j\pm\frac{1}{2}}^n = \frac{\Delta t^2}{\Delta y^2} \gamma_{i,j\pm\frac{1}{2}}^{22} g_{i,j\pm\frac{1}{2}}^{n+1} \tilde{H}_{i,j\pm\frac{1}{2}}^n, \quad (36)$$

$$S_{i,j}^n = s_{i+\frac{1}{2},j}^n + s_{i-\frac{1}{2},j}^n + s_{i,j+\frac{1}{2}}^n + s_{i,j-\frac{1}{2}}^n, \quad (37)$$

$$b_{i,j}^n = \tilde{H}_{i,j}^n - \frac{\Delta t}{\Delta x} \left[F_{i+\frac{1}{2},j}^{1,n} - F_{i-\frac{1}{2},j}^{1,n} \right] - \frac{\Delta t}{\Delta y} \left[F_{i,j+\frac{1}{2}}^{2,n} - F_{i,j-\frac{1}{2}}^{2,n} \right]. \quad (38)$$

It is clear from (34) that the linear part is symmetric and diagonally dominant, hence semi-positive definite. Furthermore, the resulting stencil is composed by at most five non zero elements, which is very convenient from a computational point of view. This is valid irrespective of $\gamma^{\alpha\beta}$, but simply due to its structure. Hence, the previous system can be rewritten in the following even more compact form

$$\tilde{H}(\eta) + T\eta = b, \quad (39)$$

that is nothing but a weakly non-linear system. This kind of system can be solved using an efficient Newton algorithm, whose convergence is guaranteed in a finite number of iterations, ([Brugnano and Casulli, 2009](#)). In summary, we are interested in the value of η such that $f(\eta) = \tilde{H}(\eta) + T\eta - b = 0$. Starting from $\xi^{(0)} > b$ we set the iteration stage as

$$\xi^{(l+1)} = \xi^{(l)} - \left[G^{(l)} + T \right]^{-1} \left[\tilde{H}(\xi^{(l)}) + T\xi^{(l)} - b \right] \quad l = 0, 1, 2, \dots \quad (40)$$

where

$$G_{i,j}^{(l)} = \left. \frac{d\tilde{H}}{d\xi} \right|_{i,j} = \begin{cases} \sqrt{\gamma}_{i,j} & \text{if } \xi_{i,j}^{(l)} > b_{i,j} \\ 0 & \text{otherwise,} \end{cases} \quad (41)$$

The stopping criteria is then $|f(\xi^{(l)})| < \epsilon$ where ϵ can be chosen as small as $\epsilon = 10^{-10}$. This algorithm implicitly includes and solves the non linearities associated to the wetting and drying, that is automatically embedded in the implicit solver. An alternative high order approach to solve this problem for the shallow water system was proposed by [Xing et al. \(2010\)](#).

Comments and remarks:. The quantities $\sqrt{\gamma}$ and $\gamma_{\alpha\beta}$ may become function of η when η is dimensionally comparable to the characteristic geometrical size of the manifold. In this case we can consider $\gamma_{\alpha\beta}$ and $\sqrt{\gamma}$ as the vertically averaged quantities using the trapezoidal rule, i.e.

$$\sqrt{\gamma} \approx \frac{1}{2} [(\sqrt{\gamma})(\eta^n) + (\sqrt{\gamma})(b)]. \quad (42)$$

Concerning the term $(\sqrt{\gamma})(\xi)$ appearing in $H(\xi)$ and its Jacobian $G^{(l)}$ it may be written as

$$G_{i,j}^{(l)} = \left. \frac{d\tilde{H}}{d\xi} \right|_{i,j} = \left. \frac{d}{d\xi} (\sqrt{\gamma}(\xi) \max(0, \xi - b)) \right|_{i,j} = \begin{cases} \sqrt{\gamma}_{i,j} + (\xi_{i,j} - b_{i,j}) \frac{d\sqrt{\gamma}}{d\xi} & \text{if } \xi_{i,j}^{(l)} > b_{i,j} \\ 0 & \text{otherwise,} \end{cases} \quad (43)$$

that is a simple linearization of $\sqrt{\gamma}$. Since $\sqrt{\gamma}$ is a known function we can also use its analytical expression to better approximate $G_{i,j}^{(l)}$. Note also that, even if Δx and Δy are constant in the reference space, their contribution in the non-linear system is not constant when γ becomes a function of the coordinates. In the spherical coordinate system, for example, this would lead to larger velocities in the coordinate space with respect to the physical one.

3.3. Pixel resolution

We want now to extend the algorithm using subgrids for the bathymetry and the fluxes, following [Casulli \(2019\)](#). The idea is that, even if the free surface elevation can be approximated using large cells, the bathymetry needs to be approximated with a finer mesh. In a Cartesian framework we then define a new quantity

$$\tilde{b}_{i,j,i_s,j_s} := b \left(x_{i-\frac{1}{2}} + (i_s - 0.5) \frac{\Delta x}{N_x^s}, y_{j-\frac{1}{2}} + (j_s - 0.5) \frac{\Delta y}{N_y^s} \right) \quad \forall i_s = 1 \dots N_x^s \quad j_s = 1 \dots N_y^s, \quad (44)$$

where N_x^s and N_y^s are the number of sub-intervals inside each computational cell. For simplicity we assume these quantities constant for every element. Of course if $N_x^s = N_y^s = 1$ then the definition of \tilde{b} coincides with the one adopted in (25). We then need to generalize all the fluxes in (29) and the volumes according to this new definition

$$\tilde{b}_{i+\frac{1}{2},j,j_s} = \max(\tilde{b}_{i,j,N_x^s,j_s}, \tilde{b}_{i+1,j,1,j_s}), \quad (45)$$

$$\tilde{b}_{i,j+\frac{1}{2},i_s} = \max(\tilde{b}_{i,j,i_s,N_y^s}, \tilde{b}_{i,j+1,i_s,1}), \quad (46)$$

$$\tilde{H}_{i,j}(\eta_{i,j}^n) = \sum_{i_s=1}^{N_x^s} \sum_{j_s=1}^{N_y^s} \frac{\sqrt{\gamma}_{i,j}}{N_x^s N_y^s} \max(0, \eta_{i,j}^n - \tilde{b}_{i,j,i_s,j_s}), \quad (47)$$

$$\tilde{H}(\eta_{i+\frac{1}{2},j}^n) = \sum_{j_s=1}^{N_y^s} \frac{\sqrt{\gamma}_{i+\frac{1}{2},j}}{N_y^s} \max(0, \eta_{i+\frac{1}{2},j}^n - \tilde{b}_{i+\frac{1}{2},j,j_s}), \quad (48)$$

$$\tilde{H}(\eta_{i,j+\frac{1}{2}}^n) = \sum_{i_s=1}^{N_x^s} \frac{\sqrt{\gamma}_{i,j+\frac{1}{2}}}{N_x^s} \max(0, \eta_{i,j+\frac{1}{2}}^n - \tilde{b}_{i,j+\frac{1}{2},i_s}). \quad (49)$$

Of course the Jacobian of $\tilde{H}(\xi)$ should be computed accordingly and reads

$$G_{i,j}^{(l)} = \sum_{i_s=1}^{N_x^s} \sum_{j_s=1}^{N_y^s} \frac{\sqrt{\gamma_{i,j}}}{N_x^s N_y^s} \mathcal{H}(\xi_{i,j}^{(l)} > \tilde{b}_{i,j,i_s,j_s}) \quad (50)$$

where $\mathcal{H}(l)$ is the Heaviside function. The structure of the resulting non-linear system is essentially the same, the Newton algorithm is then guaranteed to converge in a finite number of iterations (Casulli, 2019), since N_x^s and N_y^s are finite if the initial guess satisfy $\xi_{i,j} > \max_{i_s,j_s} \tilde{b}_{i,j,i_s,j_s}$ for all i and j .

3.4. Explicit non linear terms

We need now to specify the computation of $F_{i+\frac{1}{2},j}^{1,n}$ and $F_{i,j+\frac{1}{2}}^{2,n}$ for each $i = 1 \dots N_x$ and $j = 1 \dots N_y$. Concerning the pure convective step, any conservative explicit scheme can be used, such as a simple upwind (Ferrari and Dumbser, 2021). However this would lead to a time step restriction based on the local coordinate velocity. In order to obtain an unconditionally stable method, here we use a simple semi-Lagrangian approach following the idea introduced by Stelling and Duinmeijer (2003), and more recently by Tavelli et al. (2022) and Casulli (2026). Namely we adopt a simple semi-Lagrangian approach based on a modified advection speed as depicted in Fig. 2. First we compute a new field $v_{i+\frac{1}{2},j}^{1,*}$ and $v_{i,j+\frac{1}{2}}^{2,*}$ using $v_{i+\frac{1}{2},j}^1$, $v_{i,j+\frac{1}{2}}^2$ and $\tilde{H}_{i,j}^n$, see Tavelli et al. (2022) for details. Then, for every interface $(i + \frac{1}{2}, j)$, we move backward until the foot of the Lagrangian trajectory. The velocity field at the foot, $(v^{1,fl}, v^{2,fl})$, is then obtained using a simple interpolation of the surrounding velocities. Then we can simply set

$$F_{i+\frac{1}{2},j}^{1,n} = v^{1,fl} \tilde{H}_{i+\frac{1}{2},j}^n \quad F_{i,j+\frac{1}{2}}^{2,n} = v^{2,fl} \tilde{H}_{i,j+\frac{1}{2}}^n. \quad (51)$$

The metric correction from the right hand side of Eq. (12) is added to (51) in the form of an explicit

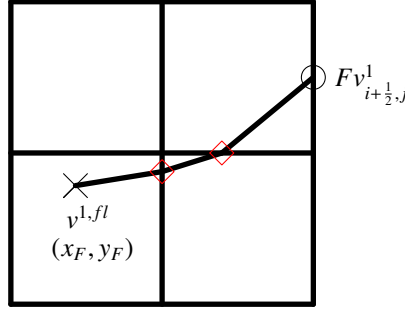


Figure 2: Lagrangian trajectory in the uniform mesh.

contribution:

$$F_{i+\frac{1}{2},j}^{1,n} = v^{1,fl} \tilde{H}_{i+\frac{1}{2},j}^n + \frac{\Delta t}{2} \gamma_{i+\frac{1}{2},j}^{11} \left[\left(v_{i+\frac{1}{2},j}^{1,n} \right)^2 (\partial_1 \gamma_{11})(x_{i+\frac{1}{2}}, y_j) + \left(v_{i+\frac{1}{2},j}^{2,n} \right)^2 (\partial_1 \gamma_{22})(x_{i+\frac{1}{2}}, y_j) \right] \tilde{H}_{i+\frac{1}{2},j}^n \quad (52)$$

$$F_{i,j+\frac{1}{2}}^{2,n} = v^{2,fl} \tilde{H}_{i,j+\frac{1}{2}}^n + \frac{\Delta t}{2} \gamma_{i,j+\frac{1}{2}}^{22} \left[\left(v_{i,j+\frac{1}{2}}^{1,n} \right)^2 (\partial_2 \gamma_{11})(x_i, y_{j+\frac{1}{2}}) + \left(v_{i,j+\frac{1}{2}}^{2,n} \right)^2 (\partial_2 \gamma_{22})(x_i, y_{j+\frac{1}{2}}) \right] \tilde{H}_{i,j+\frac{1}{2}}^n. \quad (53)$$

The Coriolis force can then be added by solving the advective-Coriolis subsystem (20)-(21) or better, by considering also the metric correction terms as an additional explicit part of the subsystem (20)-(21).

3.5. Scaling for large scale simulations

When this covariant approach is applied to the full earth, a proper rescaling of the equation becomes necessary, since the quantities in Eq. (5) are in the order of 10^{13} in the standard units of meters. In order to see how the rescaling works, let first explicit the factor $\sqrt{\gamma}$ in the PDE system (9)-(10):

$$\partial_t(\sqrt{\gamma}H) + \partial_\beta(\sqrt{\gamma}Hv^\beta) = 0, \quad (54)$$

$$\partial_t(\sqrt{\gamma}Hv_\alpha) + \partial_\beta(\sqrt{\gamma}Hv_\alpha v^\beta) + g\sqrt{\gamma}H\partial_\alpha\eta = \frac{1}{2}\sqrt{\gamma}Hv^\mu v^\nu \partial_\alpha\gamma_{\mu\nu}. \quad (55)$$

In spherical coordinates, $\sqrt{\gamma} = R^2 \sin \theta$, hence it is convenient to divide both the continuity and the momentum equation by the reference radius R^2 . The new system reads

$$\partial_t(\sqrt{\tilde{\gamma}}H) + \partial_\beta(\sqrt{\tilde{\gamma}}Hv^\beta) = 0, \quad (56)$$

$$\partial_t(\sqrt{\tilde{\gamma}}Hv_\alpha) + \partial_\beta(\sqrt{\tilde{\gamma}}Hv_\alpha v^\beta) + g\sqrt{\tilde{\gamma}}H\partial_\alpha\eta = \frac{1}{2}\sqrt{\tilde{\gamma}}Hv^\mu v^\nu \partial_\alpha\gamma_{\mu\nu}, \quad (57)$$

where

$$\tilde{\gamma}_{\alpha\beta}(\theta, \phi) = \frac{1}{R^2} \begin{pmatrix} R^2 & 0 \\ 0 & R^2 \sin^2 \theta \end{pmatrix} = \begin{pmatrix} 1 & 0 \\ 0 & \sin^2 \theta \end{pmatrix} \quad (58)$$

is a rescaled metric tensor. It is worth mentioning that this practical approach amounts to the replacement $\sqrt{\gamma} \rightarrow \sqrt{\tilde{\gamma}}$, while the transformation among covariant and contravariant components is still performed using the true metric given by Eq. (5). Several practical tests have shown that this pragmatic procedure is quite efficient, and the Newton algorithm is able to handle the equations with a reasonable tolerance, namely $tol_N = 10^{-8}$, for all the considered test cases.

3.6. Algorithm adaptation to arterial flows

In this section we want to show that a classical semi-implicit scheme for arteries can be obtained directly from the proposed algorithm using cylindrical coordinates and an appropriate re-interpretation of the gravity force. Let us start from the PDE system written with the explicit contribution of the metric as in Eq. (54)-(55) and with the metric in standard cylindrical coordinates:

$$\gamma_{\alpha\beta} = \begin{pmatrix} 1 & 0 \\ 0 & R^2 \end{pmatrix} \quad \sqrt{\gamma} = R, \quad x^1 = z, x^2 = \theta. \quad (59)$$

It is clear that if we want to represent an elastic pipe, expansions or contractions of the pipe will be modeled through a change of the metric along the radial direction, which, in our two-dimensional framework, corresponds to the passive direction, see Fig. 3. For convenience, we use the same definitions introduced by Casulli et al. (2012a) and Lucca et al. (2023) for arteries. The pressure is related to the radius through the expression $p = p_e + \beta(R - R_0)$ where β is a rigidity coefficient (Casulli et al., 2012a). In Lucca et al. (2023) this relation was expressed in terms of an area as

$$p = p_e + k \left(\sqrt{\frac{A}{A_0}} - 1 \right) = p_e + \frac{k}{\sqrt{A_0}} (\sqrt{A} - \sqrt{A_0}) = p_e + \frac{k}{R_0} (R - R_0) = p_e + \beta(R - R_0), \quad (60)$$

where we have defined $\beta = k/R_0$. If we combine Eq. (60) with the hydrostatic approximation adopted throughout this paper, i.e. $p - p_e = \rho g \eta$, we obtain

$$R = R_0 + \frac{1}{\beta}(p - p_e) = R_0 + g\rho_0 \frac{\eta}{\beta} = R_0 + \eta, \quad (61)$$

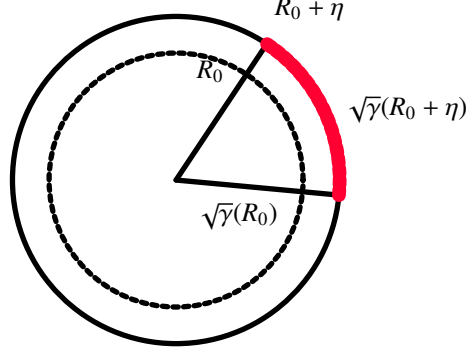


Figure 3: Draft of the cylindrical geometry and metric

where we have re-defined $g = \beta/\rho_0$. The net effect of this approach is that the metric acquires a dependence on η which expresses the deformation of the tube:

$$\gamma_{\alpha\beta}(z, \theta, R_0, \eta) = \begin{pmatrix} 1 & 0 \\ 0 & (R_0 + \eta)^2 \end{pmatrix} \quad \sqrt{\gamma} = R_0 + \eta = R \quad \frac{\partial \sqrt{\gamma}}{\partial \eta} = 1. \quad (62)$$

As usual, we compute $H(\eta) = \max(0, \eta - b)$ and we can set $b = -R_0$. In this way the bottom collapses to the inner center, and the fluid flow fills the entire cylinder, which is prone to deformations. In addition, $H(\eta) = \max(0, \eta + R_0) = \max(0, R)$. Since the metric is no longer constant, we use a simple trapezoidal rule to approximate the metric term along the radial direction, namely

$$\sqrt{\gamma} \approx \frac{1}{2} \left(\sqrt{\gamma}|_{\eta=-R_0} + \sqrt{\gamma}|_{\eta} \right) = \frac{R}{2}. \quad (63)$$

Neglecting the advection and gravity gradient contributions, Eq. (54)-(55) become:

$$\partial_t \left(\frac{R^2}{2} \right) + \partial_z \left(\frac{R^2}{2} v^z \right) + \partial_\theta \left(\frac{R^2}{2} v^\theta \right) = 0, \quad (64)$$

$$\partial_t \left(\frac{R^2}{2} v_z \right) = -g \frac{R^2}{2} \partial_z \eta \quad (65)$$

$$\partial_t \left(\frac{R^2}{2} v_\theta \right) = -g \frac{R^2}{2} \partial_\theta \eta. \quad (66)$$

Integrating the first equation for $\theta \in [0, 2\pi]$ and $z = [z_{i-\frac{1}{2}}, z_{i+\frac{1}{2}}]$ and assuming periodic boundaries we obtain

$$\begin{aligned} \Delta z \partial_t (\pi R^2) + \left(\pi R^2 v^z \right)_{z=z_{i+\frac{1}{2}}} - \left(\pi R^2 v^z \right)_{z=z_{i-\frac{1}{2}}} + \Delta z \left(\frac{R^2}{2} v^\theta \right)_{\theta=2\pi} - \Delta z \left(\frac{R^2}{2} v^\theta \right)_{\theta=0} &= 0 \\ \implies \partial_t (\pi R^2) + \frac{\left(\pi R^2 v^z \right)_{z=z_{i+\frac{1}{2}}} - \left(\pi R^2 v^z \right)_{z=z_{i-\frac{1}{2}}}}{\Delta z} &= 0, \end{aligned} \quad (67)$$

which is a consistent integral form of the mass conservation expressed as

$$\partial_t A + \pi \partial_z (R^2 v^z) = 0. \quad (68)$$

This shows that we can obtain the one-dimensional elastic tube as a particular case when $g = \beta/\rho_0$, taking the metric tensor (62) with $N_\theta = 1$ and $\Delta\theta = 2\pi$. Note that, since now the quantity $\tilde{H}(\eta) = \sqrt{\gamma}(\eta) \max(0, \eta - b)$ is in the form of (43), then its gradient (50) becomes, with pixel resolution,

$$\mathbf{G}_{i,j}^{(l)} = \sum_{i_x=1}^{N_x^s} \sum_{j_s=1}^{N_y^s} \left[\frac{\sqrt{\gamma}(\xi_{i,j}^{(l)})}{N_x^s N_y^s} \mathbf{1}(\xi_{i,j}^{(l)} > \tilde{b}_{i,j,i_s,j_s}) + \frac{1}{N_x^s N_y^s} \left(\frac{\partial \sqrt{\gamma}}{\partial \eta} \right) (\xi_{i,j}^{(l)}) \max(0, \xi_{i,j}^{(l)} - \tilde{b}_{i,j,i_s,j_s}) \right]. \quad (69)$$

For a proper comparison with a classical solver like in Lucca et al. (2023), we need to compute the pressure $p^{n+1} - p_e = g\rho\eta^{n+1} = \beta\eta^{n+1}$. We stress that, by allowing for $N_\theta > 1$, the algorithm is not restricted to axially symmetric flows but it is able to handle non-axisymmetric configurations, such as those that are produced when the coefficient β (and hence g) has a dependence on the angle θ .

4. Numerical tests

4.1. Smooth wave propagation over waterland

In this section we want to test a simple smooth wave propagation at very large scales. In particular, we are interested in the behavior of a travelling wave when it crosses the poles, where the metric factor $\sqrt{\gamma} \rightarrow 0$. In this framework, even if the real velocity of the fluid is moderate, the coordinate velocity may be very large to compensate the distortion due to the metric. We assume the metric in our standard spherical coordinates:

$$\gamma_{\alpha\beta}(\theta, \phi, R) = \begin{pmatrix} R^2 & 0 \\ 0 & R^2 \sin^2 \theta \end{pmatrix} \quad (70)$$

with $R = 6.371 \cdot 10^6 m$ and the total height is assumed negligible with respect to this manifold, i.e. $\tilde{H} \ll R$. To do so, the bathymetry is taken constant on the entire sphere and it is equal to $b = -7000m$. For this test, Coriolis force is deactivated. The initial conditions are given by a simple Gaussian profile centered in $\theta_0 = 160^\circ 00' 00''$ and $\phi_0 = -35^\circ 00' 00''$ which corresponds to the standard latitude and longitude given by $70^\circ S$ and $35^\circ W$. The shape of the free surface is then defined by

$$\eta(\theta, \phi) = 10e^{-\ell^2(\theta, \phi, \theta_0, \phi_0)/\sigma^2}, \quad (71)$$

with $\sigma = 2 \cdot 10^5 m$, where $\ell(\theta, \phi, \theta_0, \phi_0)$ is the geodetic distance among two points on the surface defined by the coordinates (θ, ϕ) and (θ_0, ϕ_0) .

The coordinate space is then defined by $\Omega_R = [0, \pi] \times [0, 2\pi]$ and it is covered by $N_x = 200$ and $N_y = 400$ elements. For the time discretization we use $\Delta t = 100s$. The resulting celerity is $c = \sqrt{gH} \approx 262.049 m/s$. Note that an explicit discretization of the celerity would be limited by this remarkably high velocity. We consider $t_{end} = 8 \times 10^4 s$ with a sampling output time given by $\Delta t_{out} = 10^4 s \approx 2 \text{ hours } 46 \text{ min}$. In Figure 4 is reported the wave evolution in both the coordinate space and on the manifold, with snapshots at different times displayed along the rows in the figure. We also show the isolines of the geodetic distance from the original point (θ_0, ϕ_0) , that corresponds to the distance $c \cdot t_{out}$ meters from the source for each output time t_{out} . The circular wavefront matches very well the spatial position where it is expected to be at each output time. Moreover, no pathological behaviors occur at the poles, which are formally singular for the coordinates used, with no need to adopt special *ad hoc* treatments. This peculiar feature is the result of the Newton algorithm that is able to implicitly solve the metric singularity. In this scenario an explicit discretization, or the semi-Lagrangian scheme summarized in Sect. 3.4, are not limiting the time step size since the local fluid velocity is very small. However this is strictly related to the local conformation close to the pole. On the other hand, the Newton algorithm, which is a strategy to account for the weak nonlinearity of $H(\eta) \rightarrow 0$, is naturally extended to $\tilde{H}(\eta) \rightarrow 0$, which becomes zero at the pole thanks to the metric. Figure 5 shows the wave front when it crosses the south pole. Since the mesh is uniform in the coordinate space, it produces

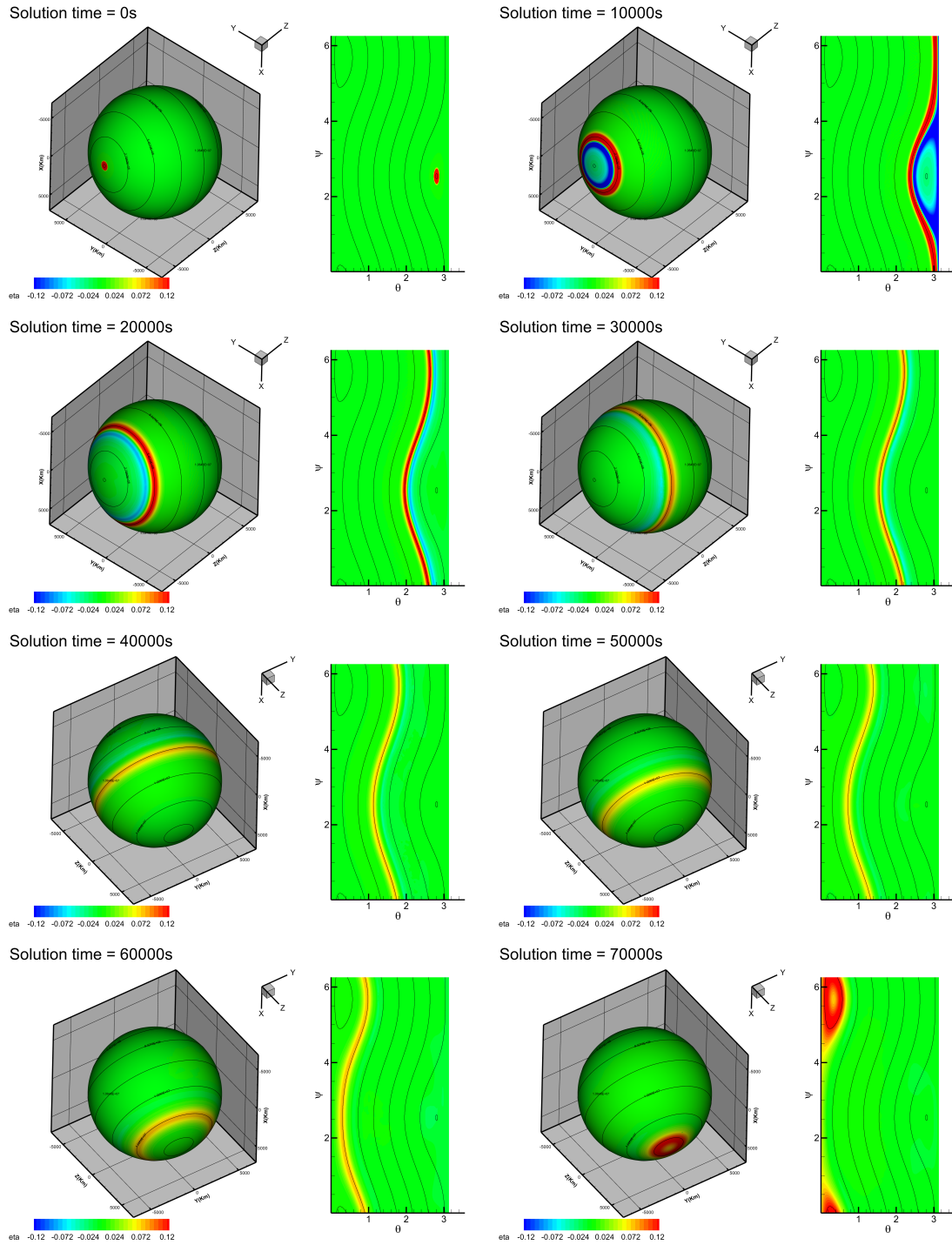


Figure 4: Time evolution of the wave at times $t = [0, 1 \times 10^4, 2 \times 10^4, 3 \times 10^4, 4 \times 10^4, 5 \times 10^4, 6 \times 10^4, 7 \times 10^4]$ s, from top left to bottom right along rows. The free surface elevation is shown both in the coordinate space and on the manifold.

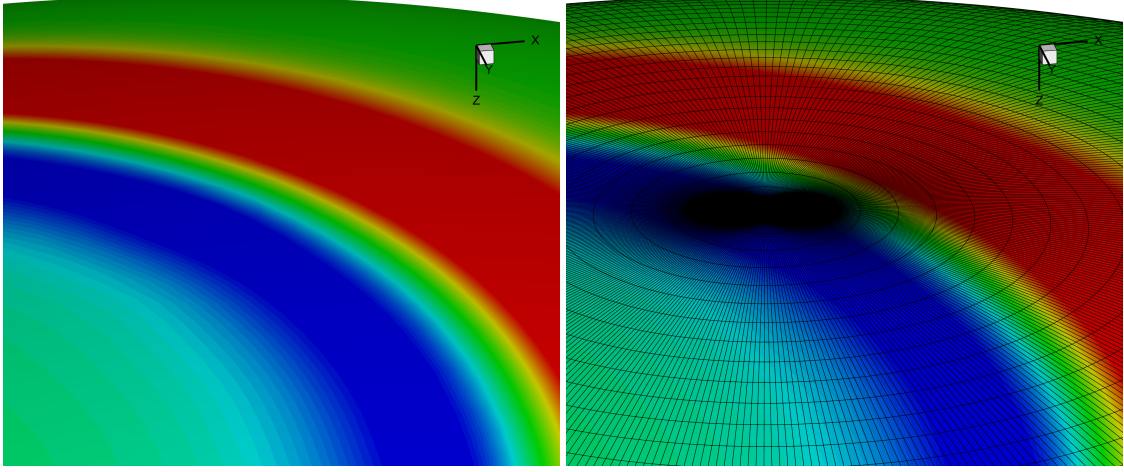


Figure 5: Detail of the numerical solution at the south pole at $t = 10^4$ s with (right panel) and without the mesh (left panel). The mesh is obtained by connecting the barycenters of each element in the coordinate space.

an extreme distortion on the manifold, however this does not affect the quality of the wave passing through it. This distortion can also be observed in the reference space (see top-right panel of Figure 4).

4.2. Well-balancing

The method proposed is by construction well-balanced in the sense of the C-property (Bermudez and Vázquez-Cendón, 1994; Castro and Parés, 2020; Gassner et al., 2016; Fernández et al., 2022) as it has been already proved by Boscheri et al. (2023a). This property is here verified on two different manifolds.

1. We first test the well-balancing property of our numerical method using a classical benchmarks, originally proposed by LeVeque (1998). In our version we consider a domain $\Omega_R = [-0.5, 0.25] \times [-0.5, 0.5]$ covered with a uniform mesh of size $N_x = 400$ and $N_y = 200$. We obtain their same effective domain by using an ad hoc non-identity metric given by

$$\gamma_{\alpha\beta} = \begin{pmatrix} 16 & 0 \\ 0 & 1 \end{pmatrix}, \quad (72)$$

so that the resulting physical space becomes $\tilde{\Omega} = [-2, 1] \times [-0.5, 0.5]$. In this way, it is also possible to check the ability of the covariant formulation using a distorted Euclidean space. The transformation in this case becomes

$$X(x, y) = \sqrt{\gamma_{11}}x \quad (73)$$

$$Y(x, y) = \sqrt{\gamma_{22}}y. \quad (74)$$

The initial condition is chosen as $v^1 = v^2 = 0$ and

$$\eta(x, y, 0) = \begin{cases} \eta_0 + \epsilon & \text{if } -0.95 \leq X(x, y) \leq -0.85, \\ 0 & \text{otherwise} \end{cases}, \quad b(x, y) = 0.8e^{-5(X(x,y)+0.1)^2 - 50Y(x,y)^2}. \quad (75)$$

We finally use a subgrid resolution of $N_x^s = N_y^s = 10$. We have run this configuration in two different set up:

Table 1: L^2 and L^∞ norm evaluated at $t = t_{end}$ for the Euclidean and the Spherical case.

Test	$L^2(\eta)$	$L^\infty(\eta)$	$L^2(u)$	$L^\infty(u)$
Euclidean	$1.1843e - 14$	$2.4425e - 14$	$7.3626e - 15$	$2.9043e - 14$
Spherical	$1.2180e - 12$	$5.0435e - 12$	$3.4542e - 14$	$3.1491e - 13$

- $\epsilon = 0.0$, $\eta_0 = 1$ and $t_{end} = 0.1$, $\Delta t = 0.001$
- $\epsilon = 0.01$, $\eta_0 = 1$ and $t_{end} = 0.48$, $\Delta t = 0.001$.

In the first setup, where η is not perturbed, we directly verify the well-balancing property. The solution at final time is shown in the left panel of Fig. 6, while the corresponding errors are reported in the first line of Tab. 1. In the second set up, with $\epsilon > 0$, we can see the interaction between the traveling wave and the bathymetry as reported in Fig. 7 at times 0.12, 0.24, 0.36 and 0.48. One can appreciate that no spurious oscillations are generated during the evolution.

2. As a second relevant configuration meant to address well balancing, we consider the entire ocean of the earth at rest, using the spherical metric tensor (70) with $R = 6.371 \cdot 10^6$ m. In this case we set $\eta_0 = 0$, while the bathymetry is built from a real Digital Elevation Model (DEM) based on the data available from GebCo (GEBCO Compilation Group, 2025). In particular, we included the GEBCO 2025 Grid, with ice surface elevation. The domain in this case is $\Omega_R = [0, \pi] \times [0, 2\pi]$, covered with $N_\theta = 200$ and $N_\phi = 400$ elements while $\Delta t = 100$ s and $t_{end} = 1000$ s. The corresponding mesh is of 1.57×10^{-2} rad for the mesh and 1.57×10^{-3} rad for the pixels, that corresponds to 100 km and 10 km at the equator, respectively. The resulting errors in L^2 and L^∞ are reported in the second line of Tab. 1. The numerical scheme is able to maintain stationarity up to machine precision, demonstrating the capability of the algorithm to reproduce the well-balancing property. For the spherical case the L^2 error is normalized with a sphere of radius 1, i.e. the element size is computed as $A(\theta, \phi) = \Delta\theta\Delta\phi \sqrt{\gamma(\theta, \phi, 1)}$ and the real value should be rescaled with the factor R^2 . However in this case the L^∞ shows that we are close to machine precision and it is only the real earth surface that generates high values. It is worth mentioning that the adopted tolerances are the same for both cases and the normalization explained in Sect. 3.5, as well as a proper preconditioner, are crucial to ensure convergence of the linear solver and of the Newton algorithm. The right panel of Fig. 6 shows the final steady solution for the *world at rest*.

4.3. Riemann problems

In order to verify the capability of the scheme to operate with different metric tensors, we consider a couple of classical Riemann problems (Toro, 1992; Berneti et al., 2008; Han and Warnecke, 2014): the dam-break over a wet bed and the dam-break over a dry bed. For this test we consider the following Euclidean metric

$$\gamma_{\alpha\beta} = \begin{pmatrix} K & 0 \\ 0 & 1 \end{pmatrix} \quad \sqrt{\gamma} = \sqrt{K}, \quad (76)$$

which is a modification of the classical Euclidean space with a distortion factor K in the x -direction. The coordinate domain is set to be $\Omega_R = [-0.5, 0.5] \times [0, 5]$ which is covered with $N_x = 250$ and $N_y = 2$ elements. We set $g = 1$ while the other parameters can be read in Table 2. The numerical results obtained for $K = 1, 2, 4$ and the two Riemann problems are reported in Fig. 8 and Fig. 9 against the exact solution taken from Ferrari and Dumbser (2021). In all the cases we can see a good agreement with the exact solution, as well as the effect produced by increasing distortion factors K .

4.4. Steady-state nonlinear zonal geostrophic flow

In order to check the correctness of our semi-implicit scheme on the full equations (11)-(12), including the Coriolis term of Sect. 2.3, we test our method against an exact solution of the shallow water on a sphere.

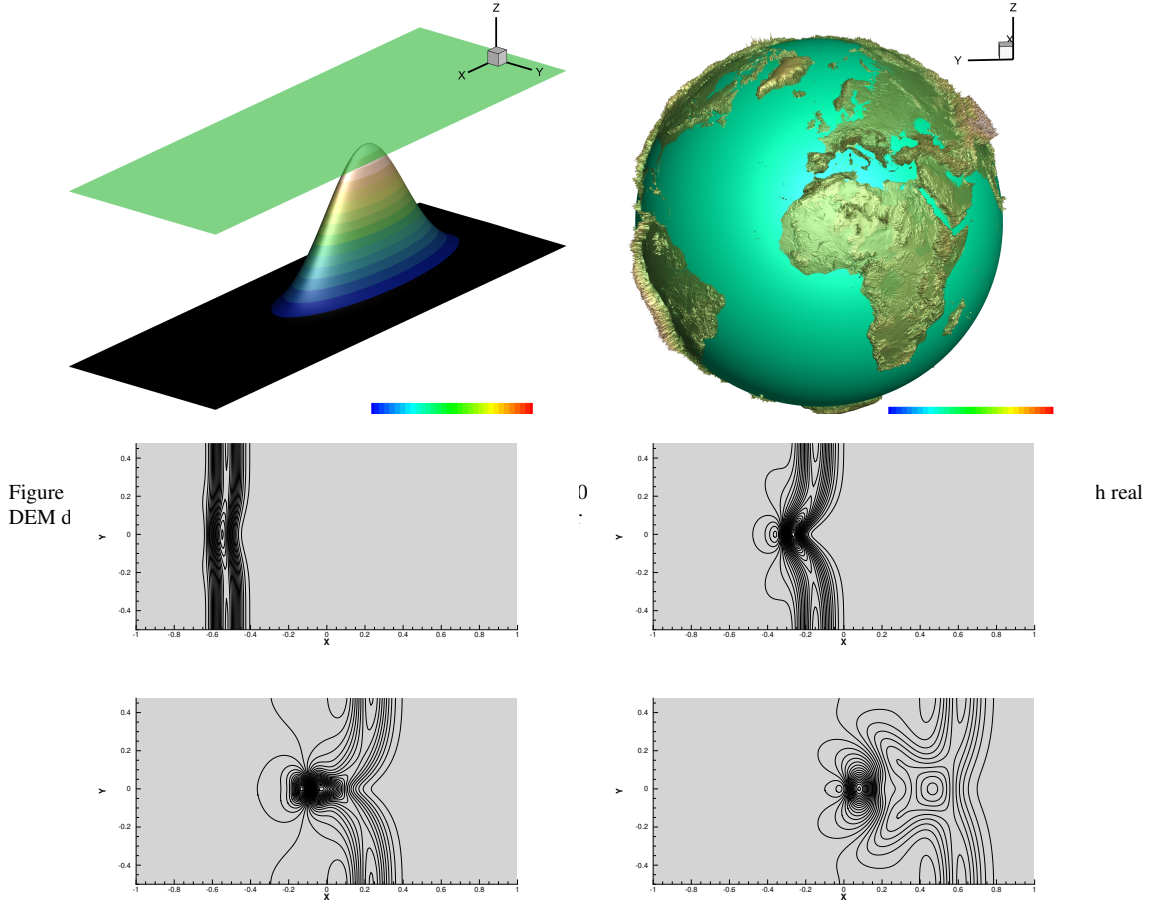


Figure 7: Numerical solution with $\epsilon = 10^{-2}$ at times $t = 0.12$, $t = 0.24$, $t = 0.36$ and $t = 0.48$, from top left to bottom right. We report the free surface elevation η through 80 equidistant contour lines ranging in the interval $\eta \in [0.99, 1.01]$.

Table 2: Parameters used in the Riemann problems.

Problem	η_L	η_R	u_L	u_R	b	t_{end}	Δt
RP1	1.0	0.1	0.0	0.0	0.0	0.25	0.0025
RP2	1.0	0.0	0.0	0.0	0.0	0.20	0.0010

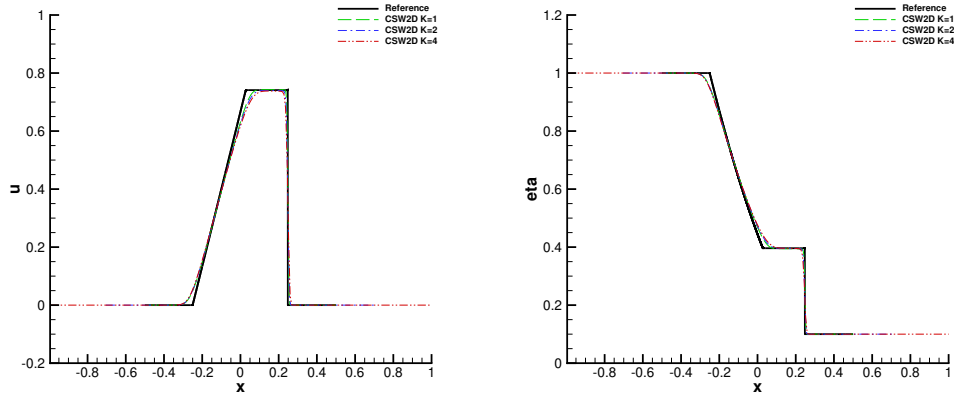


Figure 8: RP1: Comparison between the numerical and exact solution for the velocity component u (left panel) and free surface η (right panel) with different distortion factors K .

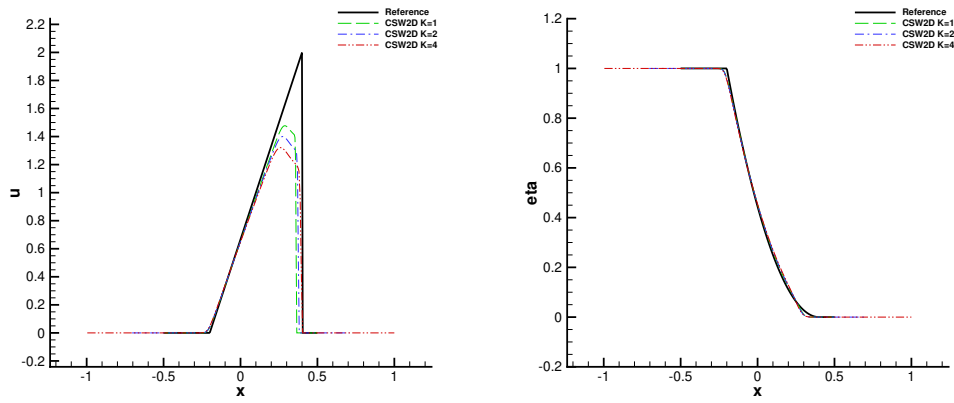


Figure 9: RP2: Comparison between the numerical and exact solution for the velocity component u (left panel) and free surface η (right panel) with different distortion factors K .

This test was proposed by [Williamson et al. \(1992\)](#) and represents a solid body rotation on a sphere where the free surface gradient is in equilibrium with the Coriolis force. The initial condition is set as

$$u(\theta, \phi, 0) = 0 \quad (77)$$

$$v(\theta, \phi, 0) = U_0 \cos\left(\theta - \frac{\pi}{2}\right) \quad (78)$$

$$\eta(\theta, \phi, 0) = \eta_0 - \frac{1}{g} \left(R\Omega U_0 - \frac{U_0^2}{2} \right) \sin^2\left(\theta - \frac{\pi}{2}\right) \quad (79)$$

$$b(\theta, \phi) = b_0. \quad (80)$$

For the sphere we use the parameters $R = 6.371 \times 10^6$ m, $\Omega_R = 2\pi/7.292 \cdot 10^{-1}$ rad/s and $U_0 = 20$ m/s which refer to the earth parameters. We cover the coordinate domain $\Omega = [0, \pi] \times [0, 2\pi]$ with a uniform mesh of size $N_x = 100$ and $N_y = 200$. We finally set $\Delta t = 100$ s and $t_{end} = 10^4$ s. The resulting free surface and velocity field at the final time are reported in [Fig. 10](#), top left panel, for a three dimensional view. The remaining panels of [Fig. 10](#), on the other hand, allow for a closer comparison to the exact solution, by showing the velocity field and the free surface elevation, along one dimensional profiles. In order to quantify the impact of the Coriolis force, we have run the same simulation by removing its presence in the equations. It is clear from [Fig. 10](#) that the Coriolis force has a huge impact on the entire domain, and neglecting its contribution leads to un-tolerable errors.

4.5. Pressure gradient over an artery branch

In this section we want to simulate an artery branch. As a reference we take the RP1 in [Lucca et al. \(2023\)](#). According to the notation of [Sect. 3.6](#), we use $k_{ref} = k = 2.005 \cdot 10^4$ Pa, $A_0 = 3.14 \cdot 10^{-4}$ m². The initial pressure is expressed in terms of the difference between the reference area and the initial area ([Lucca et al., 2023](#)). In particular $A_L = f_L A_0$ and $A_R = f_R A_0$. The pressure may be derived as $p_L = k(\sqrt{f_L} - 1)$ and $p_R = k(\sqrt{f_R} - 1)$ and then $\eta_L = p_L/\beta$, $\eta_R = p_R/\beta$ with $\beta = k/R_0 = 2.001 \cdot 10^6$ Pa/m. Setting $\rho_0 = 1050$ kg/m³ we get a uniform $g = 1.9057 \cdot 10^3$ m/s². The metric tensor is expressed by [Eq. \(62\)](#) with $b = -R_0$, which is kept constant along the tube. A close comparison of our numerical results with those reported in [Lucca et al. \(2023\)](#) can be obtained by simply inverting the previous formula, to get

$$p = \beta\eta \quad \frac{A}{A_0} = \frac{\pi(R_0 + \eta)^2}{A_0} \quad f[ml/s] = \pi(\eta + R_0)^2 u. \quad (81)$$

In our test we use $\Omega_R = [0, 0.2] \times [0, 2\pi]$ covered with $N_r = 400$, $N_\theta = 50$. The left and the right axial velocities are taken as in ([Lucca et al., 2023](#)): $u_L = 1$ m/s, $u_R = 2$ m/s, while zero angular velocity is considered. The final time is set to $t_{end} = 0.013$ s and $\Delta t = 10^{-4}$ s. [Figure 11](#) shows the mesh with the deformation of the tube (top left panel), as well as a few relevant profiles of the solution at the final time, with a direct comparison with [Lucca et al. \(2023\)](#). In our case the data is reported for all the 50 angles. Due to the homogeneity of the tube, the flow remains axially symmetric all along the simulation, but in general this is not required, i.e. $\eta = \eta(r, \theta)$. Our algorithm shows an excellent agreement with respect to the exact solution of the problem.

5. Conclusions

We have presented a new covariant formulation of the shallow water equations, see [Eqs. \(11\)-\(12\)](#), which minimizes the formal corrections with respect to the classical form in Cartesian coordinates. In particular, no Christoffel symbol enters the equations. The new formulation is quite general, allowing for applications to arbitrary three-dimensional manifolds, although in this paper we have limited our attention to two-dimensional manifolds covered by orthogonal coordinates, hence with a diagonal metric. The equations

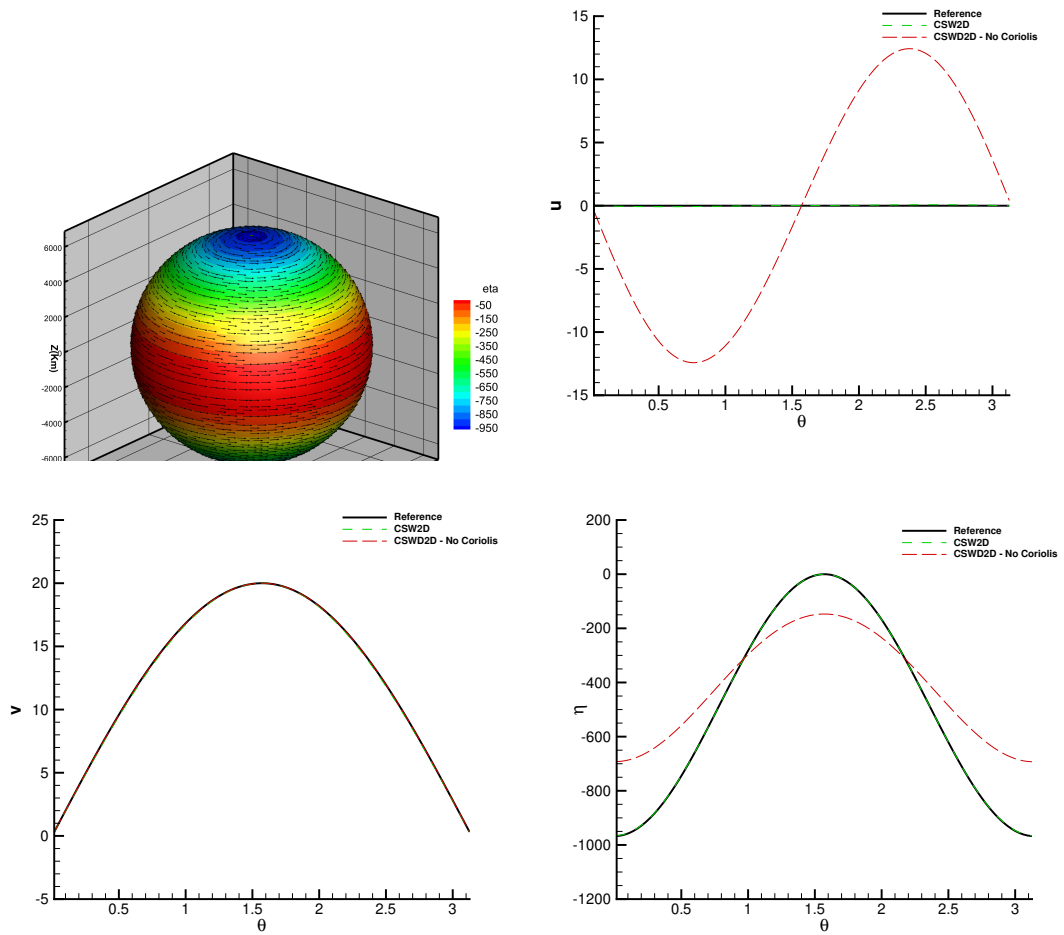


Figure 10: Top left panel: Free surface elevation and velocity field at $t_{end} = 10^4$ s; Comparison of the numerical solution with and without the Coriolis effects against the exact steady solution for the velocity field and free surface η in the remaining panels.

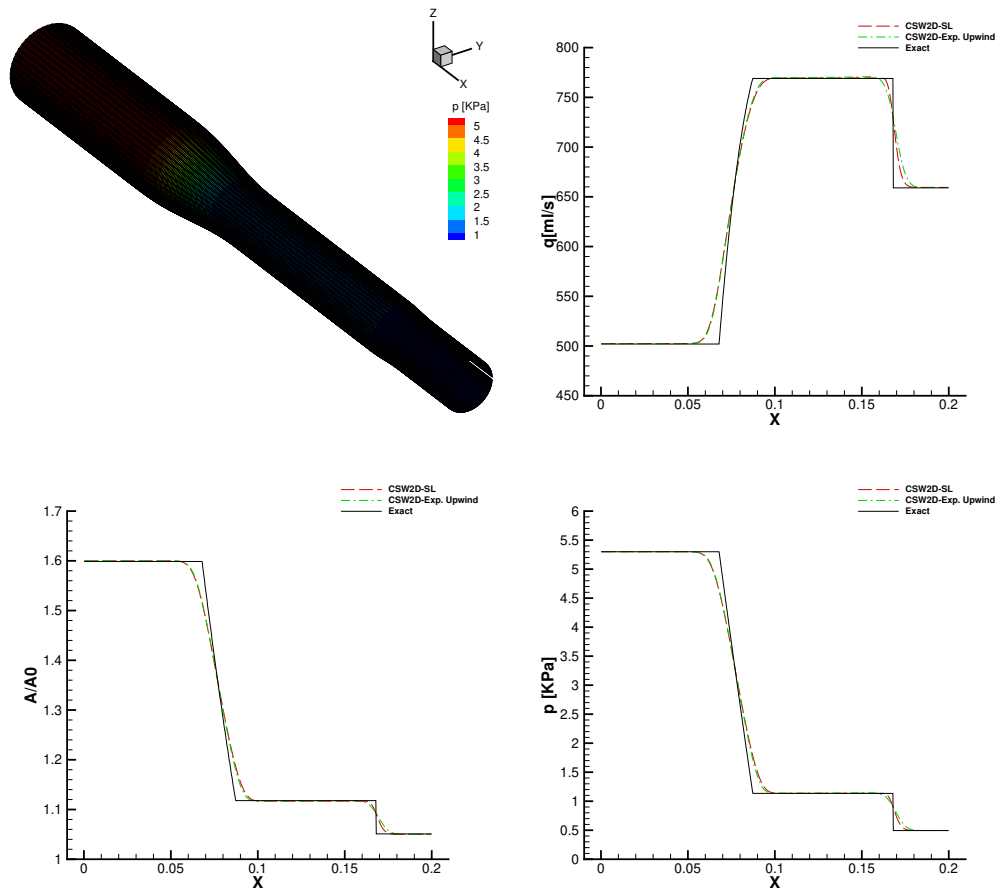


Figure 11: 3D view of the tube and its deformation, mass flow, non-dimensional cross-sectional area and pressure, at the final time $t = 0.013$ respectively from top left to bottom right.

have been discretized by means of the semi-implicit schemes developed over the years by Casulli and collaborators (see [Casulli and Zanolli \(2022\)](#) for a review). The computational approach is particularly efficient and it combines the following key features

- An implicit discretization for the gradient of surface elevation in the momentum equations and for the velocity in the continuity equation.
- The capability of treating coordinate singularities (such as those at the earth poles) by means of the same Newton approach that accounts for wetting and drying in flat geometries.
- A natural well-balancing property to preserve stationary solutions up to machine precision.
- The possibility of activating a sub-grid discretization for a higher accurate representation of the bathymetry.

The new approach has been verified over a number of stringent tests for the classical shallow water equations, including: the propagation of a smooth wave over waterland across the poles, the well balanced property of the entire earth oceans, standard Riemann problems, the simulation of a steady state geostrophic flow and the simulation of blood flow in an artery with deformation. In particular, the method can handle coordinate singularities (such as those at the poles in spherical coordinates) with no need to introduce any special treatment, but simply due to a few built-in properties that are inherent to the numerical scheme: a semi-Lagrangian discretization of the advective terms, and precise mass conservation in a wetting and drying framework.

Because of its flexibility, several more realistic applications become possible, such as oceanographic simulations of the entire planet, as well as the modeling of the full artery system.

6. Acknowledgments

We are deeply indebted to Prof. Vincenzo Casulli, whose ideas and intuitions have inspired our investigation. M.T. gratefully acknowledges the support received from the European Union with the ERC Starting Grant *ALcHyMiA* (grant agreement No. 101114995). Views and opinions expressed are however those of the author only and do not necessarily reflect those of the European Union or the European Research Council Executive Agency. Neither the European Union nor the granting authority can be held responsible for them. M.T. is also member of the INdAM GNCS group in Italy;

Appendix A. Derivation of Eqs. (9)-(10).

The continuity equation (6) is first integrated along the vertical direction, dividing by the constant term ρ . We immediately get:

$$\frac{\partial H}{\partial t} + \nabla_\beta m^\beta = 0. \quad (\text{A.1})$$

Now we use the standard expression for the covariant divergence of a generic vector m^α ([Schutz, 1980](#))

$$\nabla_\beta m^\beta = \frac{1}{\sqrt{\gamma}} \partial_\beta (\sqrt{\gamma} m^\beta), \quad (\text{A.2})$$

which allows to obtain Eq. (9). We now focus on the momentum equation (7). Due to the incompressibility assumption, we can move u^β into the covariant derivative, to obtain

$$\frac{\partial u^\alpha}{\partial t} + \nabla_\beta (u^\beta u^\alpha) + \nabla_\beta (p \gamma^{\alpha\beta}) = 0. \quad (\text{A.3})$$

We then average along the vertical direction (i.e. normally to the manifold), performing the same approximations of local velocities with their vertically averages as in [Casulli and Zanolli \(2022\)](#), recalling that $v^\alpha = \frac{1}{H} \int_b^\eta u^\alpha dz$

$$\implies (\text{vertical averaging}) \quad \frac{\partial(Hv^\alpha)}{\partial t} + \nabla_\beta(Hv^\beta v^\alpha) + \gamma^{\alpha\beta} \int_b^\eta \nabla_\beta [g(\eta - z)] dz = 0, \quad (\text{A.4})$$

$$\implies (\text{expand integration}) \quad \frac{\partial(Hv^\alpha)}{\partial t} + \nabla_\beta(Hv^\beta v^\alpha) + \gamma^{\alpha\beta} \left[\nabla_\beta \int_b^\eta g(\eta - z) dz + g(\eta - b) \delta_\beta b \right] \quad (\text{A.5})$$

$$\implies (\text{use } H = \eta - b) \quad \frac{\partial(Hv^\alpha)}{\partial t} + \nabla_\beta(Hv^\beta v^\alpha) + \nabla_\beta \left(\frac{1}{2} g H^2 \gamma^{\alpha\beta} \right) + g H \gamma^{\alpha\beta} \delta_\beta b = 0, \quad (\text{A.6})$$

$$\implies (\text{use } m^\alpha = H v^\alpha) \quad \frac{\partial m^\alpha}{\partial t} + \nabla_\beta \left(\frac{m^\beta m^\alpha}{H} + \frac{1}{2} g H^2 \gamma^{\alpha\beta} \right) + g H \gamma^{\alpha\beta} \delta_\beta b = 0. \quad (\text{A.7})$$

The above equation is the same as Eq. (1b) by [Carlino and Gaburro \(2023\)](#). At this point we introduce the auxiliary symmetric tensor $\tilde{T}^{\alpha\beta} = \frac{m^\alpha m^\beta}{H} + \frac{1}{2} g H^2 \gamma^{\alpha\beta}$ and we recall the fundamental identity for the covariant divergence of any symmetric tensor, i.e. [see Sect. 2.7.5 in [Carmeli \(2001\)](#)]

$$\nabla_\beta \tilde{T}_\alpha^\beta = \frac{1}{\sqrt{\gamma}} \partial_\beta (\sqrt{\gamma} \tilde{T}_\alpha^\beta) - \frac{1}{2} \tilde{T}^{\mu\nu} \partial_\alpha \gamma_{\mu\nu}. \quad (\text{A.8})$$

We also recall the fundamental identity which follows from $\nabla_\alpha \gamma_{\mu\nu} = 0$, namely

$$\gamma^{\mu\nu} \partial_\alpha \gamma_{\mu\nu} = 2 \frac{\partial_\alpha \sqrt{\gamma}}{\sqrt{\gamma}}. \quad (\text{A.9})$$

Hence Eq. (A.7), written with covariant indices, provides

$$\frac{\partial m_\alpha}{\partial t} + \nabla_\beta \left(\frac{m^\beta m_\alpha}{H} + \frac{1}{2} g H^2 \delta_\alpha^\beta \right) + g H \partial_\alpha b = 0, \quad (\text{A.10})$$

$$\implies (\text{use Eq. (A.8)}) \quad \frac{\partial m_\alpha}{\partial t} + \frac{1}{\sqrt{\gamma}} \partial_\beta \left(\sqrt{\gamma} \frac{m^\beta m_\alpha}{H} + \sqrt{\gamma} \frac{1}{2} g H^2 \delta_\alpha^\beta \right) - \frac{1}{2} \left(\frac{m^\mu m^\nu}{H} + \frac{1}{2} g H^2 \gamma^{\mu\nu} \right) \partial_\alpha \gamma_{\mu\nu} + g H \partial_\alpha b = 0, \quad (\text{A.11})$$

$$\implies (\text{multiply by } \sqrt{\gamma}) \quad \frac{\partial(\sqrt{\gamma} m_\alpha)}{\partial t} + \partial_\beta \left(\sqrt{\gamma} \frac{m^\beta m_\alpha}{H} \right) + \frac{1}{2} \partial_\alpha (g \sqrt{\gamma} H^2) - \frac{1}{2} \sqrt{\gamma} \frac{m^\mu m^\nu}{H} \partial_\alpha \gamma_{\mu\nu} - \frac{1}{4} \sqrt{\gamma} g H^2 \gamma^{\mu\nu} \partial_\alpha \gamma_{\mu\nu} + \sqrt{\gamma} g H \partial_\alpha b = 0, \quad (\text{A.12})$$

$$\implies (\text{use Eq. (A.9)}) \quad \frac{\partial(\sqrt{\gamma} m_\alpha)}{\partial t} + \partial_\beta \left(\sqrt{\gamma} \frac{m^\beta m_\alpha}{H} \right) + \frac{1}{2} g \partial_\alpha (\sqrt{\gamma} H^2) + \frac{1}{2} \sqrt{\gamma} H^2 \partial_\alpha g - \frac{1}{2} \sqrt{\gamma} \frac{m^\mu m^\nu}{H} \partial_\alpha \gamma_{\mu\nu} - \frac{1}{2} g H^2 \partial_\alpha \sqrt{\gamma} + \sqrt{\gamma} g H \partial_\alpha b = 0, \quad (\text{A.13})$$

$$\implies (\text{clean terms}) \quad \frac{\partial(\sqrt{\gamma} m_\alpha)}{\partial t} + \partial_\beta \left(\sqrt{\gamma} \frac{m^\beta m_\alpha}{H} \right) + g \sqrt{\gamma} H \partial_\alpha \eta = \frac{1}{2} \sqrt{\gamma} \left[\frac{m^\mu m^\nu}{H} \partial_\alpha \gamma_{\mu\nu} - H^2 \partial_\alpha g \right], \quad (\text{A.14})$$

which coincides with Eq. (10) in the text, except for the last term on the right hand side of Eq. (A.14) expressing the gravity gradient. Such a term, which has been intentionally omitted in Eq. (10), is very important for simulating tidal waves and its effects will be considered in a dedicated work.

References

- [1] Arpaia, L., Ricchiuto, M., Filippini, A.G., Pedreros, R., 2022. An efficient covariant frame for the spherical shallow water equations: Well balanced dg approximation and application to tsunami and storm surge. *Ocean Modelling* 169, 101915.
- [2] Bermudez, A., Vázquez-Cendón, M., 1994. Upwind methods for hyperbolic conservation laws with source terms. *Computers & Fluids* 23, 1049–1071.
- [3] Bernetti, R., Titarev, V., Toro, E., 2008. Exact solution of the riemann problem for the shallow water equations with discontinuous bottom geometry. *Journal of Computational Physics* 227, 3212–3243.
- [4] Boscheri, W., Chiozzi, A., Carlino, M.G., Bertaglia, G., 2023a. A new family of semi-implicit finite volume/virtual element methods for incompressible flows on unstructured meshes. *Computer Methods in Applied Mechanics and Engineering* 414, 116140.
- [5] Boscheri, W., Tavelli, M., Castro, C.E., 2023b. An all froude high order imex scheme for the shallow water equations on unstructured voronoi meshes. *Applied Numerical Mathematics* 185, 311–335.
- [6] Brugnano, L., Casulli, V., 2009. Iterative solution of piecewise linear systems and applications to flows in porous media. *SIAM Journal on Scientific Computing* 31, 1858–1873.
- [7] Carlino, M.G., Gaburro, E., 2023. Well balanced finite volume schemes for shallow water equations on manifolds. *Applied Mathematics and Computation* 441, 127676.
- [8] Carmeli, M., 2001. *Classical fields: general relativity and gauge theory*.
- [9] Castro, C.E., Toro, E.F., Käser, M., 2012. Ader scheme on unstructured meshes for shallow water: simulation of tsunami waves. *Geophysical Journal International* 189, 1505–1520.
- [10] Castro, M., Gallardo, J., López, J., Parés, C., 2008. Well-balanced high order extensions of Godunov’s method for semilinear balance laws. *SIAM Journal on Numerical Analysis* 46, 1012–1039.
- [11] Castro, M.J., de Luna, T.M., Parés, C., 2017a. Chapter 6 - Well-balanced schemes and path-conservative numerical methods, in: *Handbook of Numerical Analysis*. Elsevier. volume 18, pp. 131–175.
- [12] Castro, M.J., Ortega, S., Parés, C., 2017b. Well-balanced methods for the shallow water equations in spherical coordinates. *Computers & Fluids* 157, 196–207.
- [13] Castro, M.J., Parés, C., 2020. Well-balanced high-order finite volume methods for systems of balance laws. *Journal of Scientific Computing* 82, 1–48.
- [14] Casulli, V., 1990. Semi-implicit finite difference methods for the two-dimensional shallow water equations. *Journal of Computational Physics* 86, 56–74.
- [15] Casulli, V., 2009. A high-resolution wetting and drying algorithm for free-surface hydrodynamics. *International Journal for Numerical Methods in Fluids* 60, 391–408.
- [16] Casulli, V., 2019. Computational grid, subgrid, and pixels. *International Journal for Numerical Methods in Fluids* 90, 140–155.
- [17] Casulli, V., 2026. A semi-implicit numerical method for simultaneous fluid-structure interaction. *International Journal for Numerical Methods in Fluids* 98, 138–147.

- [18] Casulli, V., Dumbser, M., Toro, E., 2012a. Semi-implicit numerical modeling of axially symmetric flows in compliant arterial system. *Int J Numer Method Biomed Eng* 28, 257–72.
- [19] Casulli, V., Dumbser, M., Toro, E.F., 2012b. Semi-implicit numerical modeling of axially symmetric flows in compliant arterial systems. *International Journal for Numerical Methods in Biomedical Engineering* 28, 257–272.
- [20] Casulli, V., Walters, R.A., 2000. An unstructured grid, three-dimensional model based on the shallow water equations. *International Journal for Numerical Methods in Fluids* 32, 331–348.
- [21] Casulli, V., Zanolli, P., 2022. A review on advanced numerical methods for free-surface hydrodynamics. *Annali dell’Universita’ di Ferrara* 68, 621–643.
- [22] Courant, R., Friedrichs, K., Lewy, H., 1928. Über die partiellen Differenzgleichungen der mathematischen Physik. *Mathematische Annalen* 100, 32–74.
- [23] Delis, A.I., Nikolos, I.K., 2021. Shallow water equations in hydraulics: Modeling, numerics and applications. *Water* 13.
- [24] Dumbser, M., Casulli, V., 2013. A staggered semi-implicit spectral discontinuous galerkin scheme for the shallow water equations. *Appl. Math. Comput.* 219, 8057–8077.
- [25] Dumbser, M., Thomann, A., Tavelli, M., Boscheri, W., 2026. A structure-preserving semi-implicit four-split scheme for continuum mechanics. *Journal of Computational Physics* 559.
- [26] Fernández, E.G., Díaz, M.J.C., Dumbser, M., de Luna, T.M., 2022. An arbitrary high order well-balanced ad-er-dg numerical scheme for the multilayer shallow-water model with variable density. *Journal of Scientific Computing* 90.
- [27] Ferrari, D., Dumbser, M., 2021. A mass and momentum-conservative semi-implicit finite volume scheme for complex non-hydrostatic free surface flows. *International Journal for Numerical Methods in Fluids* 93, 2946–2967.
- [28] García-Navarro, P., Murillo, J., Fernández-Pato, J., Echeverribar, I., Morales-Hernández, M., 2019. The shallow water equations and their application to realistic cases. *Environmental Fluid Mechanics* 19, 1235–1252.
- [29] Gassner, G.J., Winters, A.R., Kopriva, D.A., 2016. A well balanced and entropy conservative discontinuous galerkin spectral element method for the shallow water equations. *Applied Mathematics and Computation* 272, 291–308.
- [30] GEBCO Compilation Group, 2025. Gebco gridded bathymetry data. <https://www.gebco.net/data-products/gridded-bathymetry-data>.
- [31] Han, E., Warnecke, G., 2014. Exact riemann solutions to shallow water equations. *Quarterly of Applied Mathematics* 72, 407–453.
- [32] Ii, S., Xiao, F., 2010. A global shallow water model using high order multi-moment constrained finite volume method and icosahedral grid. *Journal of Computational Physics* 229, 1774–1796.
- [33] Kolar, R.L., Gray, W.G., Westerink, J.J., Jr., R.A.L., 1994. Shallow water modeling in spherical coordinates: equation formulation, numerical implementation, and application. *Journal of Hydraulic Research* 32, 3–24.
- [34] LeVeque, R., 1998. Balancing source terms and flux gradients in high-resolution Godunov methods: the quasi-steady wave-propagation algorithm. *Journal of Computational Physics* 146, 346–365.

- [35] Lucca, A., Busto, S., Müller, L., Toro, E., Dumbser, M., 2023. A semi-implicit finite volume scheme for blood flow in elastic and viscoelastic vessels. *Journal of Computational Physics* 495, 112530.
- [36] Lucca, A., Müller, L., Fraccarollo, L., Toro, E., Dumbser, M., 2025. On simple well-balanced semi-implicit and explicit numerical methods for blood flow in networks of elastic vessels with applications to ffr prediction. *Journal of Computational Physics* 538.
- [37] Mihalas, D., Weibel-Mihalas, B., 1984. *Foundations of Radiation Hydrodynamics*. Oxford University Press, New York.
- [38] Montoya, T., Rueda-Ramírez, A.M., Gassner, G.J., 2026. Entropy-stable discontinuous spectral-element methods for the spherical shallow water equations in covariant form. *Journal of Computational Physics* 555, 114782.
- [39] Ndengna Ngatcha, A.R., 2024. High order shallow water equations: application to dam break problems. *Journal of Mechanics* 40, 820–842.
- [40] Ringler, T., Thuburn, J., Klemp, J., Skamarock, W., 2010. A unified approach to energy conservation and potential vorticity dynamics for arbitrarily-structured c-grids. *Journal of Computational Physics* 229, 3065–3090.
- [41] Schutz, B.F., 1980. *Geometrical methods of mathematical physics*. Cambridge University Press.
- [42] Stelling, G.S., Duinmeijer, S.P.A., 2003. A staggered conservative scheme for every froude number in rapidly varied shallow water flows. *International Journal for Numerical Methods in Fluids* 43, 1329–1354.
- [43] Tavelli, M., Boscheri, W., Stradiotti, G., Pisaturo, G.R., Righetti, M., 2022. A mass-conservative semi-implicit volume of fluid method for the navierstokes equations with high order semi-lagrangian advection scheme. *Computers and Fluids* 240, 105443.
- [44] Tavelli, M., Dumbser, M., 2014. A high order semi-implicit discontinuous galerkin method for the two dimensional shallow water equations on staggered unstructured meshes. *Applied Mathematics and Computation* 234, 623–644.
- [45] Tavelli, M., Dumbser, M., Casulli, V., 2013. High resolution methods for scalar transport problems in compliant systems of arteries. *Applied Numerical Mathematics* 74, 62–82.
- [46] Toro, E.F., 1992. Riemann problems and the waf method for solving the two-dimensional shallow water equations. *Philosophical Transactions of the Royal Society of London, Series A: Physical and Engineering Sciences* 338, 43–68.
- [47] Toro, E.F., 2024. *The Shallow Water Equations*. Springer Nature Switzerland, Cham. pp. 1–13.
- [48] Williamson, D.L., Drake, J.B., Hack, J.J., Jakob, R., Swarztrauber, P.N., 1992. A standard test set for numerical approximations to the shallow water equations in spherical geometry. *Journal of Computational Physics* 102, 211–224.
- [49] Wintermeyer, N., Winters, A.R., Gassner, G.J., Kopriva, D.A., 2017. An entropy stable nodal discontinuous galerkin method for the two dimensional shallow water equations on unstructured curvilinear meshes with discontinuous bathymetry. *Journal of Computational Physics* 340, 200–242.
- [50] Xing, Y., Zhang, X., Shu, C.W., 2010. Positivity-preserving high order well-balanced discontinuous galerkin methods for the shallow water equations. *Advances in Water Resources* 33, 1476–1493.

- [51] Zeitlin, V., 2007. Chapter 1 introduction: Fundamentals of rotating shallow water model in the geophysical fluid dynamics perspective, in: Zeitlin, V. (Ed.), *Nonlinear Dynamics of Rotating Shallow Water: Methods and Advances*. Elsevier Science. volume 2 of *Edited Series on Advances in Nonlinear Science and Complexity*, pp. 1–45.